Research Article | Vol. 10, No. 3 | 1 Mar 2019 | BIOMEDICAL OPTICS EXPRESS 1234
Biomedical Optics EXPRESS

Contrast improvement in indocyanine green fluorescence sensing in thick tissue using a time-gating method

GORO NISHIMURA*

Research Institute for Electronic Science, Hokkaido University, N20W10, Sapporo 001-0020, Japan
*gnishi@imd.es.hokudai.ac.jp

Abstract: Indocyanine green-based fluorescence imaging techniques are very powerful in clinical applications, but the imaging is restricted to the signal from the near-surface region of tissue. Here, we focus on the method to discriminate the fluorescence signal from the background using a time-domain gating technique. The contrast of the fluorescence image from a fluorescence object at more than 1 cm depth in a meat phantom could be enhanced about 4–5 times relative to the continuous wave method if the time-gate range was properly selected. Further, a Monte Carlo simulation with a simple background model indicates that a shorter source and detector distance is more effective to improve the contrast. The simple time-gating method will enable a highly sensitive fluorescence detection in thick tissue.

1. Introduction

The detection of clinically specific fluorescence signal in thick tissues is very important in advanced medical applications. For example, the detection of the sentinel lymphonodes (SLNs) during the breast cancer surgery is one of the keys to improve the clinical outcome for the patients after the surgery [1]. There are several methods to visualize SLNs using the blue dye method, the indocyanine green (ICG) dye-based fluorescence angiography and the radioisotope (RI) injection. The former two optical methods are beneficial for reducing the cost and limitation of the facilities but the detection is only limited to a shallow region of tissue. In contrast, the RI methods are very sensitive but there are large problems such as the exposure to RIs, the facility and the cost. Therefore, new technologies free from the drawback of the RI method are highly demanded for the detection of SLNs in thick tissues. One of the current procedure is the intraoperative sensing of SLNs using a small gamma ray detection probe. The clinician is interactively searching the origin of the RIs, which are accumulated in SLNs [2]. Further, the procedure is sometimes conducted with the blue dye method or the ICG method to help the resection by clinician and the results are quite successful [3].

The fluorescence technique here is basically a near-infrared (NIR) fluorescence imaging by a charge coupled device (CCD) camera or an intensified CCD camera with planar illumination. These devices are commercially available and actually using in many cases [4]. However, the detection depth is limited to around 1 cm because of the strong scattering and the absorption by tissue [5, 6], and thus the RI method is still a standard method. The photo acoustic imaging (PAI) is also focused to overcome the problems of the RI method. There are many demonstration studies *in vitro* and *in vivo* with small animals [7] and a pioneering study with human subject has been reported recently [8]. The depth sensitivity of PAI is considerably high and the wide depth range is the most important advantage of this method among other optical methods. However, the sensitivity to the contrast agents seems to be low compared with that of the fluorescence technique [9]. The multimodal approach using PAI, fluorescence imaging and ultrasound guidance is also proposed to combine the advantages of these modalities [10]. Nevertheless, these new technologies have been extensively studied.

#335407 https://doi.org/10.1364/BOE.10.001234
Journal © 2019 Received 18 Jun 2018; revised 6 Dec 2018; accepted 2 Jan 2019; published 12 Feb 2019

Biomedical Optics EXPRESS

The fluorescence technique is a very sensitive method to detect and evaluate the molecular information, and actually the sensitivity can be down to a single molecular level. Thus, the technique is a very common technique in biological researches. However this sensitivity is limited with only tiny volumes or the surface and can not easily be extended to bulk tissues. The use of NIR wavelength region improves the penetration depth in biological samples but still suffered by the strong scattering, absorption and the background signal when the depth of the interest becomes more than a few millimeters. As mentioned above, the camera based imaging technique has a problem of insufficient sensitivity to the fluorescence under thick tissue.

On the other hand, the imaging is not always required in the real clinical applications. In fact, the gamma ray detection probe is only showing the RI intensity and the surgeon is interactively searching the most intense position. Therefore, here, we aim to propose a high sensitive sensing method using a time-domain fluorescence technique, which is expected as an alternative method of the gamma ray detection probe. The main concern here is how the specific signal can be distinguished from the background. The time-domain method is one of the method to differentiate the specific signal from the background one. This idea is not quite new. Actually, it is a common technique in microscopy. Further, there are several imaging challenges *in vivo* using fluorescence dyes, which have a long fluorescence lifetime [11–13]. These are basically using the intensity in a later time region of the temporal profile with the sufficiently long fluorescence lifetime dyes. Another technique is using dyes, which emit fluorescence in a longer NIR wavelength region [14–16]. This technique is very attractive but needs to develop new dyes which can be administered to human subjects. If one could use such dyes, the contrast enhancement of the fluorescence image would be trivially expected. However, ICG, which is only dye approved for clinical applications, has relatively short fluorescence lifetime and low quantum yield. There is a research on the lifetime based classification of tumors [17]. But, it is still an open question whether the ICG signal is actually differentiated from the background using the time-domain method in real-time and how it can be optimized to improve the contrast.

In this paper, we have demonstrated the concept using a meat phantom. A pair of the point excitation source and fluorescence detection was used and scanned over the sample surface instead of standard method using the planar illumination. The planar illumination is expected to be suffered by the background because the background is always existing in front of the object signal. On the other hand, the detection point is not the highest background point in the pair scanning scheme because the highest background point is the excitation point. The pair scanning scheme is not common in the imaging schemes. One of interesting challenge was the development of a hand-held scanner basically using the pair scanning scheme [18, 19]. They have considered the background fluorescence to evaluate their method. In our case, we have employed the time-domain single photon counting method to improve more the sensitivity. Here the sensitivity means the ability to distinguish the fluorescence target signal from the background and thus is equivalent to the contrast in the imaging.

Then, a Monte Carlo (MC) simulation was also conducted to discuss the important properties on the contrast with different measurement schemes and to optimize the experimental condition for the contrast enhancement. To our best knowledge, no quantitative discussion on the contrast with different SD pair separations and on the comparison with the planar illumination under the existence of background has been reported. Finally, we have discussed on the contrast under the breakdown of the assumptions in the simulation, such as the finite fluorescence lifetime.

2. Experiment and simulation

2.1. Experimental setup

The block diagram of our experimental setup is shown in Fig. 1(a). The pulse laser source was a customized version of a femtosecond fiber laser at 780 nm; the output was fiber-coupled, the repetition rate was 10 MHz and the pulse width was less than 10 ps (CFL-04REF-HOK-02,

Biomedical Optics EXPRESS

CALMAR Laser, CA). The fiber output was firstly divided with ratio of 1:99 to the power monitor and then divided equally into two excitation points using single mode fiber optics at 780 nm. These outputs were coupled to 62.5 μm graded-index multimode (GI-MM) fibers. The one of the two fibers was delayed by an extra optical fiber to distinguish the two illumination points temporally. Finally, these two fibers illuminated the sample with 3.7 mW of the light power for each fiber. The fluorescence was detected by two bundled fibers (3 mm in diameter) at different points. Then, the fluorescence was selected by a long wavelength pass filter (FF01-834/LP, Semrock and 10CGA-760, Newport) and measured by a time-correlated single photon counting (TCSPC) system with hybrid photomultiplier tubes (PMA Hybrid-50, Picoquant, Berlin, Germany) and TCSPC boards (SPC-134EM, Becker & Hickl GmbH, Berlin, Germany). The excitation and detection fibers were fixed to a small black polylactic acid (PLA) resin holder to maintain the 10 mm excitation source and detection distance as shown in Fig. 1(b). The instrumental response function (IRF) was measured by a face-to-face setup of the excitation and detection fibers using an IRF measurement adapter. The adapter has one excitation fiber port and two detection fiber ports, which are tilted at a 15° to the excitation fiber axis and spaced at 32 mm from the excitation fiber end. The excitation beam was attenuated by neutral density filters and homogenized by a piece of paper in front of the fiber end to avoid the systematic errors, resulting about 10 k counts/sec measurement count rate. The IRF for the fluorescence detection was approximated by the IRF measured at the excitation wavelength.

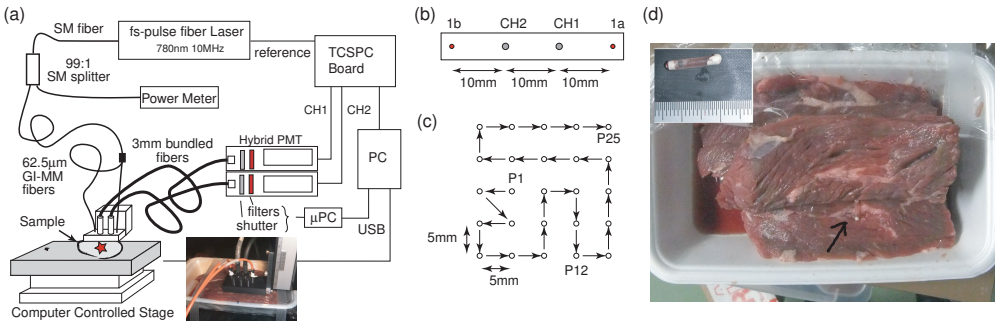

Fig. 1. Experimental setup for the phantom measurements. The time resolved system consisted in the fiber laser source, fiber optics and hybrid photomultiplier detection system with a TCSPC board (a). The source and detector fibers were fixed to a small plastic holder (b). The holder was moving on the meat surface by a motorized stage (c). The small capillary fluorescence object was implanted in the meat sample (d).

2.2. Phantom measurements

A beef meat block about 5x5x15 cm^3 was chosen to simulate human tissue because the scattering and absorption coefficients of a beef meat at the excitation wavelength 780 nm were estimated as 0.92 mm^{-1} and 0.023 mm^{-1} using a solution of diffusion equation with a half space [20] and are almost in a typical range of these coefficients of human tissues [21]. A preliminary measurement showed that the fluorescence background of the meat was also similar to that of human forearm. A small plastic tube (2 mm in inner diameter and 8 mm in length) containing a 1 μM ICG mixed to 1% Intralipid solution, which is shown in the inset picture in Fig. 1(d), was implanted at about 11 mm from the surface of the meat as a fluorescence object. The plastic fiber holder was placed in contact with the meat surface and scanned on the surface with 5 mm steps by a motorized stage in Fig. 1(b). The data were accumulated up to 90 sec. at each point to obtain temporal spread function (TPSF) of the fluorescence and then the stage was moved to the next position on the 5×5 mm^2 grid as shown in Fig. 1(c). The dark count signal of the detector, 11 to 30 counts

Biomedical Optics EXPRESS

in each time bin (6.11 ps step), was subtracted from the measured TPSFs before the analysis. In this paper, the excitation source and fluorescence detection points are represented by S and D and the pair of them is called by SD and this measurement scheme will be referred as SD pair scanning. The position is indicated by millimeter unit.

2.3. Monte Carlo simulation

A MC simulation was conducted to clarify the effect of the background to the detection of the object fluorescence. The simulation scheme was similar to a time-domain fluorescence simulation published in our previous paper [22]. The simulation code was developed from the code CUDAMCML using a general-purpose computing on graphics processing units (GPGPU) [23] and specifically modified for the time-domain fluorescence measurement with a sphere object. Further, the background fluorescence homogeneously distributed in the medium was simulated. The fluorescence properties of the background were assumed to be same to those of the fluorescence object. The fluorescence lifetime and quantum yield were assumed to be zero and the unity, respectively, to simplify the model. Our code simulated the photon, which had two states live and dead, instead of the energy packet using in the original MCML. Then, the photon path was traced until the photon was absorbed or exited from the surface. Some photons were absorbed by the fluorophore in the object and converted to the fluorescence photons and kept the tracing until absorbed or exited as shown in Fig. 2(a). The exit angle was not resolved.

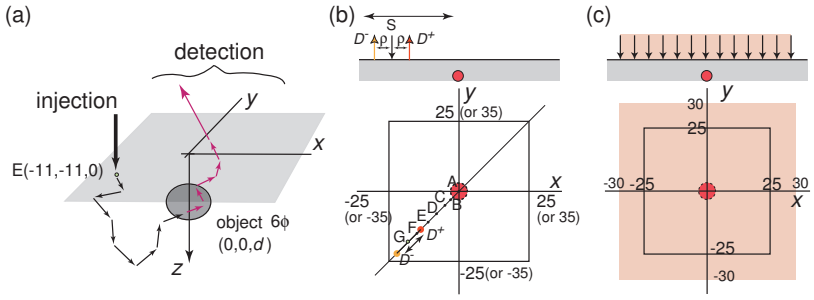

Fig. 2. Schematics of the MC simulation (a), positions of the illumination point (b) and the area of the planar illumination (c). The sphere object with 6 mm in diameter was placed at depth d under the origin. The excitation source points were moving from A (0,0) to B(-3,-3), C(-5,-5), D(-8,-8), E(-11,-11), F(-15,-15) and G(-18,-18) on the line $x = y$. The fluorescence photons were detected in each 1 mm^2 square area on the 50×50 or 70×70 mm^2 region. The TPSFs of the fluorescence at the detection points D^+ and D^- at fixed distances ρ from each source point S was analyzed. The horizontal arrow indicates the scan of these pairs on the line $x = y$ in (b). The planar illumination of the excitation was also simulated. The illumination area was placed to cover the whole detection area shown by light orange color in (c).

The optical properties for the excitation light and fluorescence of the medium were assumed to be similar to those of the tissue; the reduced scattering coefficient $\mu_s' = 1$ mm^{-1}, the absorption coefficient $\mu_a = 0.01$ mm^{-1}, the scattering anisotropy $g = 0.9$, and the refractive index $n = 1.37$ [21]. The optical properties of the object were same to the medium but the absorption of the excitation light became a sum of the base absorption and the fluorophore absorption μ_f, 0.027 mm^{-1}. The background fluorescence in the medium was set by adding the fluorophore absorption μ_{back} but the total absorption for the excitation was kept at 0.01 mm^{-1}. The object was a sphere of 3 mm radius at 11, 16 and 21 mm in depth under the origin. The measurements with different background fluorescence were also simulated; 0, 1/1000, 1/100 and 1/10 of the

Biomedical Optics EXPRESS

fluorophore absorption of the object (μ_{back}/μ_f = 0, 1/1000, 1/100 and 1/10) were chosen for the background fluorophore absorption. The direction of the injection was normal to the surface.

The excitation source point (S) was moving from A to G on the line $x = y$ and the detection points D^+ and D^- for each source point were also placed on the line $x = y$ with fixed distances at 10 and 20 mm from S to mimic the SD pair scanning in the experiments as shown in Fig. 2(b).

The fluorescence with a planar illumination of the excitation light instead of the point source illuminations was also simulated as shown in Fig. 2(c). The excitation photons were homogeneously injected from the surface plane with an area 60×60 mm^2 centered at the origin to cover the whole detection area of the simulation (50×50 mm^2). In this paper, we will call this simulation scheme as "planar illumination".

The simulations were run on workstations with GPGPUs (Tesla K20c, C2025 and C2020, Nvidia) and 2 or 4×10^{12} photons were traced.

3. Results

3.1. TPSF measurements

Figure 3(a) shows fluorescence TPSFs of a SD pair (1a-CH1) with some different positions (P1-P5,P8-P10) and IRF. The inset of the figure shows the normalized intensity ratio to the profile at P10 where the position was far from the target; $I_X(t)/I_{P10}(t) - 1$, where I_X is TPSF at position X. The intensities of the TPSFs at positions P1,P2 and P4 where the object was near the SD positions, showed higher than the others and the peak times were delayed. On the other hand, TPSFs showed quick decays and the peak moved to a faster time when the position was far from the object. The TPSF at P10 was similar to the background profile measured with another sample without the target (data not shown). The difference between the TPSFs can be more clearly shown in the inset in Fig. 3(a). The largest difference appeared in a range near 2 ns. The ratio at a region larger than 4 ns was noisy and affected by the fluctuation of the tail part of the background TPSF. The ratio profile at P8 (yellow line) did not show the peak around 2 ns and showed an unknown profile probably caused by a deviation due to the heterogeneity of the background TPSF. These results suggest that the use of the intensity near the 2 ns region will enhance the contribution of fluorescence from the object.

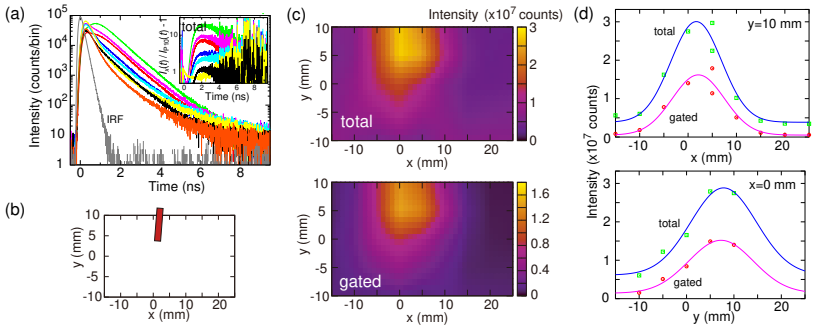

Fig. 3. TPSFs with 10 mm SD distance at different measurement points (a), approximate location of the fluorescence object (b), the total intensity and the gated intensity maps (c) and the cross section of the image at y = 10 mm and x = 0 mm (d). The TPSFs of the 1a-CH1 pair were measured at P1-P5, P8-P10, by red, green, blue, pink, cyan, yellow, black and orange solid lines, respectively. The inset shows the normalized ratio with respect to the TPSF at P10(20,0). The intensity map was depicted by the intensities using sum of the TPSF data with the total time range from -0.5 to 7.5 ns ("total") or with a selected time range at 2.05 ns ("gated") and by an interpolation of these intensities. The curves in (d) are the biased Gaussian functions fitted to the data points.

Biomedical Optics EXPRESS

Figure 3(c) shows the intensity maps obtained by the SD pair scanning. The approximated location of the fluorescence object is shown in Fig. 3(b). "Total" intensity was calculated by the sum of the TPSF data of the time range from -0.5 to 7.5 ns. This intensity is an approximation of the steady state intensity. The sum was truncated at a certain time point at 7.5 ns and therefore this intensity was slightly underestimated. The intensity of the selected time range around 2 ns was calculated by the sum of the intensity in a 2.5 ns time window centered at 2.05 ns. This intensity can be measured by a time-gate of TPSF and therefore we use "gated" to denote this scheme. The intensity of each SD position was mapped at the middle point of the pair and these intensities were spatially interpolated by gnuplot v4.6. The fluorescence intensity in the upper middle region was higher than the peripheral region. The intensity of the peripheral region mainly reflected the background level and was significantly suppressed in the gated image relative to that of the total one. The intensity profile is assumed to be a biased Gaussian function, $f(x) = a \exp[-(x - x_0)^2/2/s^2] + b$, for quantitative analysis. A 2-dimensional biased Gaussian function could fit the image (c) but the data points at y-axis did not sufficiently cover the whole profile, causing a systematic error of the bias b. Therefore, we simply fitted representative cross sections at $y = 10$ mm and $x = 0$ mm as shown in Fig. 3(d). The data points at $y = 10$ mm was fitted first by $f(x)$ to determine b and then the data point at $x = 0$ mm was fitted with b fixed to this value. The contrasts defined by the ratio a/b were then obtained as 6.7 and 31 for total and gated profiles, respectively. Therefore, about 4.6-times contrast enhancement by the gated scheme was observed at the peak position.

3.2. Simulated real-time measurements

The previous results show the contrast enhancement using a selected time range of the TPSF. However, the accumulation time of the previous measurements was 90 seconds to yield ideal TPSFs. The measurements were obviously not real-time. The real-time property of the SD pair scanning is very important in clinical applications. Since the TPSF will become more noisy because of the permitted accumulation time of each measurement is limited, the optimization of the time range is required to enhance the contrast. In this section, we generated a real-time data using previous TPSFs. We considered a near real-time condition with 100 ms acquisition time for each TPSF measurement. First, the intensity of TPSF data with 90 sec. was scaled by $1/900$ and the scaled values were assumed as the true expectation values. Then the Poisson noise was added because TCSPC data are mainly determined by Poissonian statistics [24]. The dark count was expected to be far less than 1 counts/bin and was neglected. Figure 4(a) shows the simulated TPSFs with several different positions. The dynamic range of the profile became less than 100 and very few photons were detected beyond about 4 ns but still the difference can be observed in the 2 ns range. The selection of the time range was more critical to improve the contrast. We chose the time ranges Δt from 0.5 to 2.5 ns centered at 2 ns for the comparison and obtained the cross sections of the intensity profile at $y = 10$ mm and $x = 0$ mm as shown in Fig. 4(b). The upper figures show the intensity profiles and indicate that the intensity was decreased with narrowing the time range. The error was estimated by the standard deviation of the intensity assuming Poissonian error. The profile at $y = 10$ mm was fitted first by the biased Gaussian function and then the profile at $x = 0$ mm was fitted. The profiles were well fitted by the Gaussian function. The widths s, which is the half width at the $e^{-1/2} = 0.61$ intensity, for $y = 10$ mm were 5.2 ± 0.4, 5.3 ± 0.2, 5.4 ± 0.2 and 5.4 ± 0.2 mm for total, 2.5 ns gate, 1.0 ns gate and 0.5 ns gate, respectively. There was no clear systematic dependence of the width of the profile with the different gating ranges. The width was about 5–6-times wider than the diameter of the object because of the multiple scattering. The width obtained by the profile at $x = 0$ was significantly large because the y-axis was close to the object long axis.

The profiles of the fluorescence intensity ratio to the background intensity are shown in the bottom figures in Fig. 4(b). The ratio was calculated by a/b estimated by the Gaussian fitting.

Biomedical Optics EXPRESS

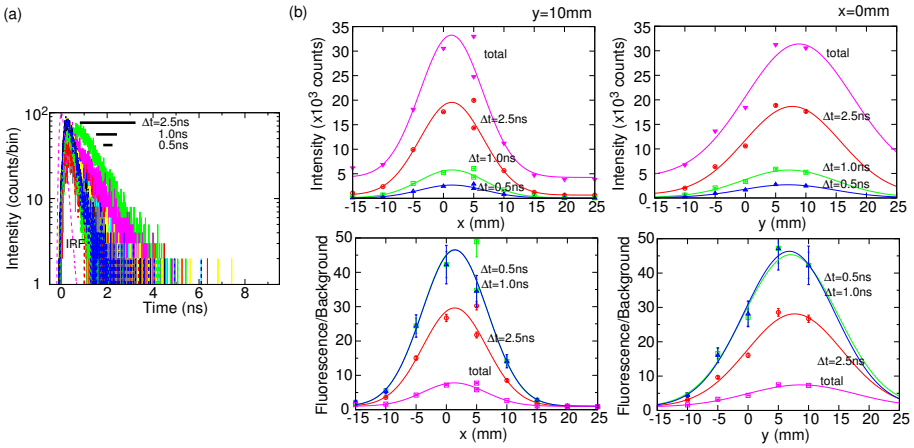

Fig. 4. The simulated TPSFs at different excitation points with 100 ms accumulation (a) and the cross section profiles at y = 10 mm and x = 0 mm of the fluorescence intensities using different time gate ranges (b). The time-gated profiles were calculated by the sum of the intensity in time ranges Δt = 0.5, 1.0 and 2.5 ns centered at 2 ns indicated by the thick solid lines in (a) and these are shown by blue, green and red symbols in (b). The total profile was calculated by the sum of the total intensity in the time range from -0.5 to 7.5 ns and is indicated by pink symbols and labeled by "total". The curve indicated by each color is the biased Gaussian function fitted to the data points. The error of the intensity was assumed as the standard deviation of the intensity. The profile of the fluorescence-background ratios was calculated by the ratio between the intensity and the bias obtained by the fitting and the error of the ratio was obtained by the error propagation rule.

The error was also estimated by the error propagation rule of the error of the intensity and the error of b. The ratio was increased with narrowing gate range but the ratio profiles at Δt = 0.5 and 1.0 ns became almost same. This is because the change of the ratio near the maximum was not large as shown in the inset in Fig. 3(a). Further, the narrowing gate range causes the large error of the ratio. The large error will make large fluctuation of the gated intensity of individual measurement and eventually the intensity change can not be distinguished from the background. The error level of the ratio profile indicates that the practical time range is expected around 2.5 ns in this case. The maximum contrast a/b was 4.7-times higher using the 2.5 ns time gate than that of the total profile. It is worth to note that the total intensity profile here is not same to the conventional fluorescence images using fluorescence cameras. This profiles was obtained by the SD pair scanning and the contrast would be expected higher than that of the conventional imaging by the following MC simulation results.

3.3. *Monte Carlo simulation of a single fluorescence object with background*

At first, the MC simulation yielded time-sliced images with 6.67 ps time step up to 3.33 ns (500-images). The images of some time slices at 0.5, 1.0, 1.5 and 2.0 ns with different object depth at 11 and 16 mm are shown in Figs. 5(a) and 5(b), respectively. The injection point was E(-11,-11) mm. The fluorescence was initially distributed at the injection point and then moved to the origin, where the object was embedded. The fluorescence with the shallow object moved quickly to the origin within 1 ns, but the fluorescence with the deeper object delayed to come that point at more than 1.5 ns later. Further, the fluorescence of the deeper object was more broadened. The background fluorescence always exists in front of the object and originates dominantly from a shallow region. As a consequence, the background fluorescence appears faster than the object because of the shorter path length. Then, the initial fluorescence is dominated by the background

Biomedical Optics EXPRESS

but later one by the object fluorescence. The object fluorescence from a deeper region is more broadened by the longer path length in the scattering medium.

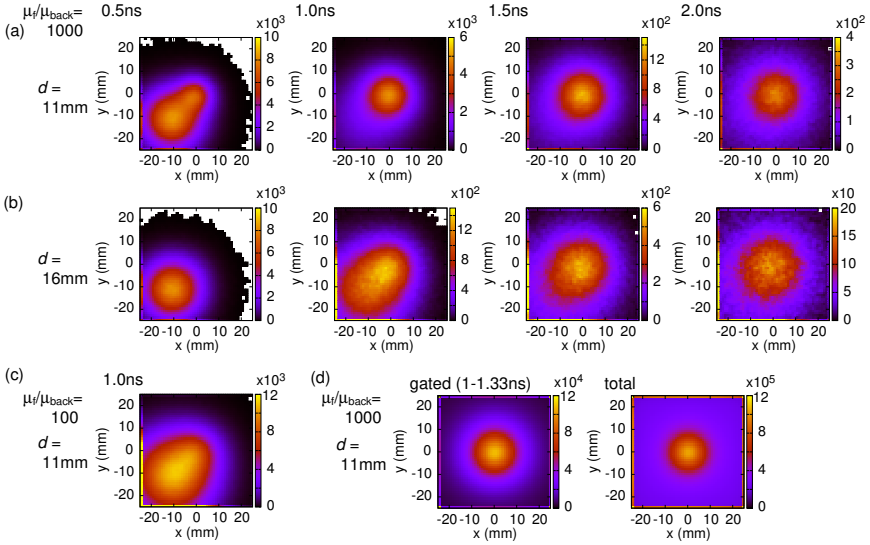

Fig. 5. Fluorescence intensity images by the MC simulations. (a) and (b) are the time slice images with the object at 11 mm and 16 mm in depth, respectively. The background fluorophore concentration was 1/1000 smaller than that of the object. (c) shows the image with the object at 11 mm but the background level was 10-times higher than that of (a) and (b). The injection points of (a)–(c) was at (-11,-11) mm. (d) shows the images with the planar illumination. The first image was the gated image using a range from 1.0 to 1.33 ns. The second image was the total intensity image using a range from 0 to 3.33 ns. The background level was 1/1000 and the object depth was 11 mm.

Figure 5(c) shows the image with a higher background level at the 1.0 ns time point with the object at 11 mm. The background was 10-times higher than that in the previous images. The fluorescence at the injection point became more intense and the object fluorescence was significantly hided by the background. It was almost difficult to distinguish the object fluorescence from much higher background level (data are not shown).

The fluorescence images with the planar illumination are shown in Fig. 5(d) to compare with the SD pair scanning measurements. The two images are corresponding to gated and total ones, which were calculated by the sum of the fluorescence intensity in a time range from 1 to 1.33 ns and by that in the whole simulation (total) time range from 0 to 3.33 ns, respectively. The total image is an approximation of the steady state image and simulates the fluorescence image by conventional measurement scheme using fluorescence cameras. The fluorescence of the total image came from the whole area and the intensity of a peripheral region was elevated because of the background. On the other hand, the time-gated image shows that the intensity of the peripheral region was suppressed and eventually the contrast of the fluorescence from the object was improved.

Figure 6 shows some TPSFs with the SD pair scanning and the intensity profile obtained by this scanning. The SD distance was 10 mm. The object fluorescence in TPSF was elevated and the center time region of the shoulder of the profile was shifted to an earlier time when the object was placed in a shallower region as shown in Fig. 6(a). In contrast, that could be only observed as a delayed shoulder in the TPSFs when the SD pair was far from the object as shown in Fig. 6(b). These results indicate that the fluorescence intensity at a later time region beyond about 1 ns always reflects more of the object fluorescence. This result qualitatively agrees with

Biomedical Optics EXPRESS

the experimental results.

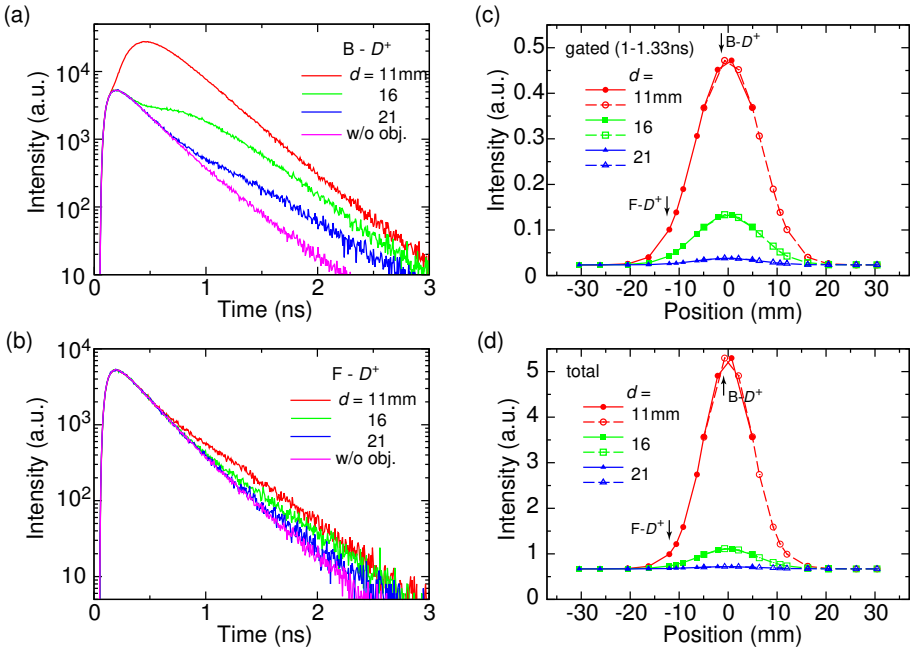

Fig. 6. Fluorescence TPSFs and intensity profiles with different depths of the object with 10 mm SD distance. (a) and (b) show some TPSFs at different SD pairs at B(-3,-3)-D^+(4,4) and F(-15,-15)-D^+(-8,-8), respectively. (c) and (d) show the profiles of the time-gated intensity in a time range from 1 to 1.33 ns and the total intensity in a time range from 0 to 3.33 ns against the different position of the SD pair scanning on the line $x = y$, respectively. The arrows in (c) and (d) indicate the middle point of each SD pair, B-D^+ and F-D^+ in (a) and (b). The profiles with dashed lines are the mirrored profiles with respect to the origin.

The intensity profiles against the position of the middle point of each SD pair are showing how the profile changes with the different object depths as shown in Figs. 6(c) and 6(d). The actual simulations was conducted with the source points on the negative half line of $x = y$ and the results are shown by the solid lines and filled symbols. Since the simulation geometry was symmetric with respect to the z-axis at the origin, the mirrored profiles are also shown by the broken lines and open symbols to visualize the whole profile. The gated intensity was about 10-times weaker than the total one. The significant decrease of the peak intensity with increase of the object depth was observed in the gated profiles but the decrease was more large in the total ones. In case of the 21 mm depth, the peak of the profile of total was not clearly visible in the figure. The intensity at a position more than 20 mm far from the origin was almost same to the background one. The background level of the gated ones was significantly suppressed from that of the total ones. As a consequence, the contrast was improved in the gated ones.

Figure 7 shows some fluorescence TPSFs and intensity profiles with different depths of the object when the planar illumination. The TPSFs at (1,1) mm and (-12,-12) mm are shown in Figs. 7(a) and 7(b), respectively. These points were selected as the nearest points to the middle points of B-D^+ and F-D^+ in Fig. 6 for comparison. The TPSFs were similar to the previous ones with the point illumination but the background response was much faster. In case of the planar illumination, the injection points distribute homogeneously on the surface. Therefore, the injection points, which are always close to the detection points, generate more photons from the region nearby the detection, resulting the fast response. The depth dependence of the TPSFs is

Biomedical Optics EXPRESS

very similar to that shown in the result with the point illumination.

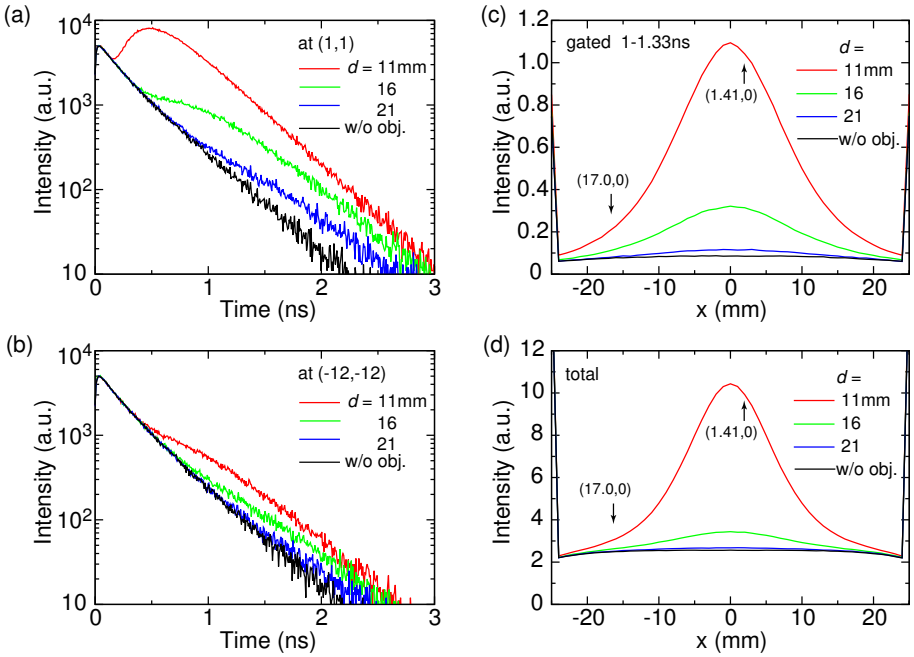

Fig. 7. Fluorescence TPSFs and intensity profiles with different depths of the object with the planar illumination. (a) and (b) show some TPSFs at different detection points at (1,1) mm and (-12,-12) mm, respectively. (c) and (d) show the profiles of the time-gated intensity in a time range from 1 ns to 1.33 ns and the total intensity in a time range from 0 ns to 3.33 ns against the different positions of the scan of the source detection pair on the line $y = 0$ mm, respectively. The arrows in (c) and (d) indicate the points, whose distances from the origin same to those of the points shown in (a) and (b). The background response and intensity profile is shown by black solid lines.

The profiles of time-gated and total intensities on the line $y = 0$ mm are shown in Figs. 6(c) and 6(d), respectively. The background profiles were not constant in the area. Actually, the intensity in the peripheral regions was smaller than the intensity at the center. This is because the area of the planar illumination was not large enough to ignore the boundaries at just 5 mm outside of the detection area. The excitation photon density is becoming small near the boundary because of no flow from the outside of the boundaries. The gated-intensity profiles were about 10-times smaller than the total ones. The total one at the 21 mm depth of the object was very close to that of the background. The qualitative properties of these profiles are very similar to those with the SD pair scan described above.

The profiles in Figs. 6 and 7 are fitted to the biased Gaussian function which was used in the analysis of the experimental data to compare the contrast and the width of the profiles. The small systematic deviation between the Gaussian curve and the profiles was found in the peak region and the tail region of the profile and more obvious at a shallower object depth. This is because the object was not a point fluorescence emitter. Figure 8 shows the contrast and width against the depth of the object with different measurement schemes, the SD pair scan with 10 and 20 mm SD distances, and the planar illumination using gated- and total intensities. The contrast and half width here are defined by a/b and s of the biased Gaussian profile, respectively. In case of the point illumination, b was firstly determined by the background simulation without the object. Then, a and s of the biased Gaussian function were determined by the fitting. The values of the

Biomedical Optics EXPRESS

bias b in the case of the 10 and 20 mm SD distances were 0.67 and 0.066 for total intensities and 0.023 and 0.009 for gated ones, respectively. The increase of the SD distance suppressed the bias level. In case of the planar illumination, the ratio of the intensities with and without the object was calculated because the background intensity was not constant due to the finite illumination area. Then the ratio was fitted by the Gaussian function with $b = 1$, yielding the contrast $a/b = a$ and the half width s.

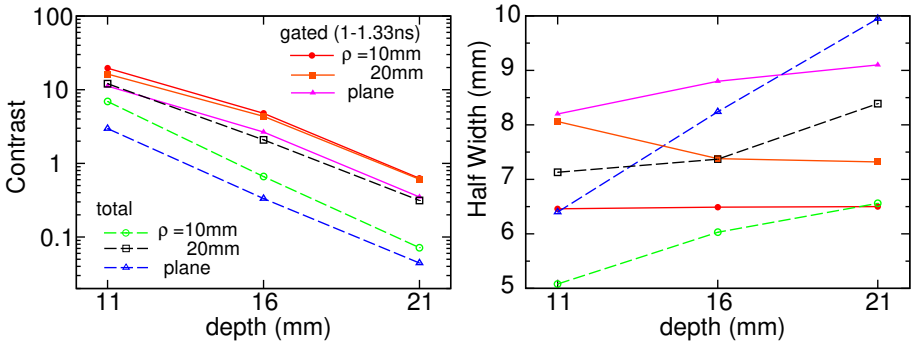

Fig. 8. The contrast and half width of the fluorescence images with different type of measurements; the SD pair scan with 10 and 20 mm distance between the SD points and the planar illumination, and each scheme using the time-gated intensity from 1 ns to 1.33 ns and the total intensity from 0 ns to 3.33 ns shown by solid and broken lines as well as filled and open symbols, respectively. The contrast and half width are defined by a/b and s in the biased Gaussian function.

The contrast of the all schemes was decreasing with the depth of the object. The contrast of the total profiles of all three schemes were smaller than those of the gated profile as shown by the broken and solid lines in the figure, respectively. The contrast with the planar illumination was always worst among these schemes. This is because the background is shining from all surface region excited by the planar illumination. The interest finding is that the contrast using a longer SD distance in the total profile is higher than using a shorter distance. On the other hand, the gated one shows opposite dependence. The background intensity is significantly attenuated with distance from the excitation point and this explains the contrast change with the total profile. On the other hand, the response of the background is delayed with the longer SD distance and overlapped more to the gated-region. Thus the contrast of the gated profile does not improve with a wider SD pair.

The width of the total profile seems to be increased with the depth but the change of the width with different schemes does not show clear systematic change. This is probably due to the difference in the agreement with Gaussian function to the profile with different scheme and depth. In case of the gated profile, the change of the width was rather small or almost constant with the 10 mm SD distance. Further, the widths is larger than those of the total one. The use of the later photon in the TPSF means that the profile is constructed with photons traveling longer path length, which lose more spatial information of the object. The fact that the width is almost constant with depths can be understood by a limited path length distribution by the time-gate.

4. Discussion

The use of the later photons in TPSFs improves the contrast of the fluorescence image with the object laying in a deep region of the medium both in the experiment and the simulation. In case of the experiment, the background might come from the Raman scattering and the autofluorescence from the optics and the meat itself. Our preliminary experiment with a living

Biomedical Optics EXPRESS

human tissue shows that the TPSF of the background was similar to that of the beef meat sample. Therefore, we speculate the similar results in *in vivo* measurements. An experimental comparison with the conventional fluorescence imaging method was not conducted because the quantitative comparison was very difficult. For instance, it is difficult to evaluate or control the parameters of the fluorescence imaging system, which are needed for the quantitative comparison, such as the heterogeneity of the excitation power in the planar illumination, the detection efficiency, and the rejection ratio of the contamination from the excitation light. These parameters are depending on individual fluorescence imaging devices and the general comparison is difficult. In this study, we conducted a fluorescence imaging measurement with the same meat sample with a circular illumination area about 4-cm in diameter with few mW of the optical power and with about 5x5 cm^2 view area using a cooled sCMOS camera (DC-152Q-FI, Andor) at about 40 cm from the sample surface. However, the fluorescence image could not distinguish the object fluorescence from the background. Therefore, we employed a MC simulation to compare between the current scheme and the conventional fluorescence imaging scheme. As expected, the contrast of the conventional fluorescence imaging is significantly lower than that obtained by the imaging with the SD pair scanning scheme. The contrasts of the conventional one are 2.97 and 0.044 with the object at 11 and 21 mm in depth, respectively. On the other hand, the contrasts with the time-gated SD pair scanning using the 10 mm SD distance are 19.6 and 0.63 at 11 and 21 mm and are 6.6 and 14.3 times higher than those of the conventional method, respectively, as shown in Fig. 8. Therefore, this significant low contrast value of the conventional imaging method can explain the difference of the result of the conventional fluorescence imaging and the time-gated measurements.

The real-time measurement feature is demanded in the real applications. In particular, the expected use of this method is the probe like an intraoperative gamma probe scanning at the patient tissue by clinicians with a much more simple but sensitive device than those developed in previous studies [18, 19]. Figure 4 shows the expected TPSFs in the near real-time condition with 100 ms accumulation time. The latter part of the TPSF shown in Fig. 3 became almost under the dark noise of the measurement about 0 count/bin. The fluorescence lifetime of the ICG sample in this measurement was 0.6 ns and very similar to the value of ICG in blood [22]. This value is luckily making the large intensity difference from the background in an about 2 ns time region of the TPSF, where some amount of photon event can be measured even with 100 ms accumulation time. However, the contrast improvement was a trade off against the statistical errors by narrowing the time gating window. The results indicate that the relatively large time window, about 2.5 ns, still works to improve the contrast.

In this study, the power density of the laser light was exceeded to the maximum permissible exposure defined in the ANSI Z136.1 because the illumination area defined by the core size of the excitation fiber, 62.5μm, was very small. However, the illumination beam size is expandable to satisfy the limit. The ANSI limit is about 3 mW/mm^2 at 785 nm with the exposure time larger than 10 s and will be satisfied by using the size larger than 1.23 mm^2 beam size. This expansion of the beam size will not change the results much because the size is small relative to the SD distance. This limitation is more relaxed by using real-time measurement because the exposure time is far less than 10 sec. and thus our exposure condition is not largely different from the condition in the real applications. Further, the amount of ICG in the target, 25 pmole (1 μM ICG in a 0.025 ml tube), seems to be significantly smaller than that in the other studies [18] and thus it is possible to use a higher concentration of the target to reduce the laser power.

The MC simulation was based on a very simplified model; the fluorescence lifetime was assumed to be infinitely small and the background and object have same fluorescence properties. The assumption on the quantum yield only affects the fluorescence intensity because the intensity is proportional to the quantum yield and the amount of the fluorophores if the absorption by the fluorophores is not too large. The heterogeneity, such as a layered structure, was ignored and the

Biomedical Optics EXPRESS

geometry of tissue was simplified using a half space in this simulation. We consider that the space size of the tissue like human chest is large enough relative to the SD separation and the simple assumption may work on such large space. The heterogeneity must be smoothed by the scattering if the SD size is sufficiently large relative to the size of the heterogeneity. The SD distance in the current simulation was 10 mm or more, which is larger than the layer structure of skin. If the SD distance becomes very small, the layer structure can not be ignored to simulate the early part of TPSF. Finally, the assumption of the lifetime is more important to be considered.

The simulation with the zero fluorescence lifetime shows the clear separation of the object fluorescence from the background one in the fluorescence profiles, because the different time profile is purely caused by the difference of the optical path length. The profile with a finite fluorescence lifetime for the object and the background will be more broadened, resulting the time-gating will be less effective. We will discuss later more. In case of the beef measurements, the background was decaying faster than the object fluorescence decay. Therefore, the finite fluorescence lifetime of the object will only change the object fluorescence response. The object fluorescence will be more delayed than the current simulation with the finite fluorescence lifetime. Therefore, the difference of TPSFs with and without the object can be observed in a more delayed time region. However, the qualitative result by the simulation will not be change. For example, the larger SD distance will not help the gain of the contrast improvement in the time-gated profile. Further, even simple SD pair scanning is expected to give better contrast relative to the typical fluorescence imaging method.

The interest finding on the contrast increase with a shorter SD distance in the time-gating scheme is very similar to the findings published in the time-domain near-infrared spectroscopy (NIRS) [25, 26]. Their finding is that the fraction of photons traveled in deeper location is increased in the photons traveled longer path length when the SD distance becomes short. Thus, the use of a time gate to select a later time region of TPSF enhances the sensitivity of the absorption at a deeper location. As a consequence, the sensitivity becomes maximum with the null distance condition of the SD pair. In case of the fluorescence imaging, the fluorescence from the object is hided by the background, which is always existing in front of the object. This situation is similar to that in NIRS, but the result in NIRS does not directly indicate our finding. The sensitivity to the fluorescence intensity of the object is maximum with the null distance because the path length to and from the object is shortest and this is easily expected. To understand the contrast, one should consider the generation of the background fluorescence and the object fluorescence. The absorption of a whole volume selected by a time-gate is the origin of the background. On the other hand, the fluorescence of the object is originated by the absorption at a deeper object location. Therefore, the contrast of the object fluorescence to the background is basically determined by the ratio of the absorption at a deeper location to that in a volume selected by the time gate. This can be explained by more precise way. Under the Born approximation scheme, the intensity change observed by a small absorption change will be given by a product of the absorption change and a convolution of two Green's functions, which describe the photon propagation from the source to the object and from the object to the detector. The fluorescence intensity is exactly given by the same form under the diffusion approximation and the assumption of zero fluorescence lifetime, the equality of the optical parameters. Under the RTE, the existence of the scattering phase function in the excitation photon propagation is different from the expression of the fluorescence and this difference could be ignored if the object is far from the detection point [22]. Therefore, the current finding can be understood as a fluorescence version of the NIRS results reported.

In the practical applications, unspecific ICG signal may be observed as a background because ICG is not designed for any specific target. In this case, a similar fluorescence lifetime value of the background to that of the object fluorescence is expected and thus the gain of the contrast improvement will be significantly reduced. This is because the background level in the time-gating

Biomedical Optics EXPRESS

range is increased by the temporal profile broadening. The impact of the finite fluorescence lifetime of the background can be roughly estimated as follows.

The asymptotic temporal profile of the background with the zero fluorescence lifetime can be given by an exponential attenuation, $\exp(-\mu_a c t)$, where μ_a is the absorption of the medium [27]. The temporal profile with the finite fluorescence lifetime τ_f is expressed by the convolution of the exponential decay function $\tau_f^{-1}\exp(-t/\tau_f)$ to the temporal profile of the zero fluorescence lifetime. Therefore, assuming this asymptotic profile, the increase of the background at a time t is roughly given by

$$B_f(t)/B_f^0(t) = 1/(1-\gamma)\{1-\exp[-(1-\gamma)t/\tau_f]\}$$

where B_f and B_f^0 are the background intensities of the finite and zero fluorescence lifetimes and $\gamma = \tau_f \mu_a c$, respectively. Using the absorption coefficient 0.01 mm^{-1} and the refractive index 1.37 in the MC simulation and the fluorescence lifetime 0.6 ns, the background will increase with a factor 2.2 at $t = 1$ ns. Therefore, the contrast using the time-gate around 1 ns becomes about half and is close to that of the total measurement with $\rho = 20$ mm. The advantage of the time-gating scheme is significantly reduced. Therefore, it is very crucial to reduce the unspecific background. The rough estimation $B_f(t)/B_f^0(t)$ also indicates that the background elevates more at a later time point. The proper selection of the time region for the gating is very important to improve the contrast. For instance, the time-gate selecting a very later time region does not improve the contrast when the background is generated by the unspecific fluorescence probes. Therefore, further optimization in the selection of the gate time region and that in the dose level and administration procedure of the probes are required to achieve the good performance in the contrast improvement by the time-gating scheme.

Almost all applications using the time-gating method are based on the selection of a later part of the fluorescence temporal response to eliminate the contribution of background because the background emission is decaying fast in many cases. Then, the design and development of long fluorescence lifetime fluorescence probes are very important. However, the above estimation indicates that the good specificity of such new probes are very crucial for the success of the time-gating method.

The optical properties of beef meat in the experiments is different from human tissues, in general. However, the scattering and absorption coefficients of a beef meat are almost in a typical range of these coefficients of human tissues [21]. On the other hand, the background emission of human tissue measurements has not been discussed in the NIR region. We speculate that the main origin of the emission from the beef meat is Raman scattering and the background from the optics and these similarly contribute human measurements. We are planing to measure human subjects to validate these issues in the next step. Further, we will also evaluate the unspecific contribution of ICG under the real clinical situations. We are also planning to conduct more realistic simulations in particular for the finite fluorescence lifetime to address the above problems to optimize the selection of the time gate and the optical setup.

5. Conclusion

The proper selection of the time window for TPSFs makes a significant improvement in the contrast of the time-gated fluorescence intensity profile with a SD scanning profile in real-time measurements. This significant improvement of the contrast will achieve very sensitive detection of the fluorescence probe in thick tissues relative to the conventional fluorescence imaging. The MC simulations qualitatively confirm the experimental profile and further indicate the better configuration about the SD distance to increase the sensitivity. An advanced simulation including more realistic situations will optimize the experimental condition to improve the method.

Biomedical Optics EXPRESS

Funding

Medical Research and Development Programs Focused on Technology Transfer (KYOUSOU) by Japan Agency for Medical Research and Development (AMED) (15im0402006h0005) and Grants-in-Aid for Scientific Research (KAKENHI) by The Ministry of Education, Culture, Sports, Science and Technology (MEXT) (JP18K18448).

Acknowledgments

The author thanks to Prof.Shigeto Ueda at Saitama Medical University for suggestions on the possible clinical applications.

Disclosures

The author declares that there are no conflicts of interest related to this article.

References

1. S. K. Somasundaram, D. W. Chicken, and M. R. Keshtgar, "Detection of the sentinel lymph node in breast cancer," Br. Med. Bull. **84**, 117–131 (2007).
2. G. Mariani, P. Erba, G. Villa, M. Gipponi, G. Manca, G. Boni, F. Buffoni, F. Castagnola, G. Paganelli, and H. W. Strauss, "Lymphoscintigraphic and intraoperative detection of the sentinel lymph node in breast cancer patients: The nuclear medicine perspective," J. Surg. Oncol. **85**, 112–122 (2004).
3. H.-C. Zeng, J.-L. Hu, J.-W. Bai, and G.-J. Zhang, "Detection of sentinel lymph nodes with near-infrared imaging in malignancies," Mol. Imaging Biol. pp. 1–9 (2018).
4. T. Kitai, T. Inomoto, M. Miwa, and T. Shikayama, "Fluorescence navigation with indocyanine green for detecting sentinel lympho nodes in breast cancer," Breast Cancer **12**, 211–215 (2005).
5. K. Polom, D. Murawa, Y. Rho, P. Nowaczyk, M. Hünerbein, and P. Murawa, "Current trends and emerging future of indocyanine green usage in surgery and oncology," Cancer **117**, 4812–4822 (2011).
6. T. Kitai and M. Kawashima, "Transcutaneous detection and direct approach to the sentinel node using auxiliary compression technique in ICG fluorescence-navigated sentinel node biopsy for breast cancer," Breast Cancer **19**, 343–348 (2012).
7. S. Zackrisson, S. M. W. Y. van de Ven, and S. S. Gambhir, "Light in and sound out: Emerging translational strategies for photoacoustic imaging," Cancer Res. **74**, 1–26 (2014).
8. A. Garcia-Uribe, T. N. Erpelding, A. Krumholz, H. Ke, K. Maslov, C. Appleton, J. A. Margenthaler, and L. V. Wang, "Dual-modality photoacoustic and ultrasound imaging system for noninvasive sentinel lymph node detection in patients with breast cancer," Sci. Reports **5**, 15748 (2015).
9. B. Wang, Q. Zhao, N. M. Barkey, D. L. Morse, and H. Jiang, "Photoacoustic tomography and fluorescence molecular tomography: A comparative study based on indocyanine green," Med. Phys. **39**, 2512–2517 (2012).
10. J. Kang, J. H. Chang, S. M. Kim, H. J. Lee, H. Kim, B. C. Wilson, and T.-K. Song, "Real-time sentinel lymph node biopsy guidance using combined ultrasound, photoacoustic, fluorescence imaging: in vivo proof-of-principle and validation with nodal obstruction," Sci. Reports **7**, 45008 (2017). .
11. R. Cubeddu, G. Canti, P. Taroni, and G. Valentini, "Time-gated fluorescence imaging for the diagnosis of tumors in a murine model," Photochem. Photobiol. **57**, 480–485 (1993).
12. J. R. Mansfield, K. W. Gossage, C. C. Hoyt, and R. M. Levenson, "Autofluorescence removal, multiplexing, and automated analysis method for *in-vivo* fluorescence imaging," J. Biomed. Opt. **10**, 041207 (2005).
13. L. Gu, D. J. Hall, Z. Qin, E. Anglin, J. Joo, D. J. Mooney, S. B. Howell, and M. J. Sailor, "*In vivo* time-gated fluorescence imaging with biodegradable luminescent porous silicon nanoparticles," Nat. Commun. **4**, 2326 (2013).
14. G. Hong, J. Z. Wu, J. T. Robinson, H. Wang, B. Zhang, and H. Dai, "Three-dimensional imaging of single nanotube molecule endocytosis on plasmonic substrates," Nat. Commun. **3**, 700 (2012).
15. G. Hong, J. C. Lee, J. T. Robinson, U. Raaz, L. Xie, N. F. Huang, J. P. Cooke, and H. Dai, "Multifunctional *in vivo* vascular imaging using near-infrared ii fluorescence," Nat. Medicine **18**, 1841–1846 (2012).
16. Y. Tsukasaki, M. Morimatsu, G. Nishimura, T. Sakata, H. Yasuda, A. Komatsuzaki, T. M. Watanabeabe, and T. Jin, "Synthesis and optical properties of emissiontunable PbS/CdS core-shell quantum dots for *in vivo* fluorescence imaging in the second nearinfrared window," RSC Adv. **4**, 41164 (2014).
17. A. T. N. Kumar, S. A. Carp, J. Yang, A. Ross, Z. Medarova, and C. Ran, "Fluorescence lifetime-based contrast enhancement of indocyanine green-labeled tumores," J. Biomed. Opt. **22**, 040501 (2017).
18. S. J. Erickson, J. Ge, A. Sanchez, and A. Godavarty, "Two-dimensional fast surface imaging using a handheld optical device: *in vitro* and *in vivo* fluorescence studies," Transl. Oncol. **3**, 16–22 (2010).
19. J. Gonzalez, J. DeCerce, S. J. Erickson, S. L. Martinez, A. Nunez, M. Roman, B. Traub, C. A. Flores, S. M. Roberts, E. Hernandez, W. Aguirre, R. Kiszonas, and A. Godavarty, "Hand-held optical imager (Gen-2): improved instrumentation and target detectability," J. Biomed. Opt. **17**, 081402 (2012).

Biomedical Optics EXPRESS

20. F. Martelli, S. Del Bianco, A. Ismaelli, and G. Zaccanti, *Light Propagation through Biological Tissue* (SPIE Press, 2009).
21. J. Mobley and T. Vo-Dinh, "Optical properties of tissue," in *Biomedical Photonics Handbook,* T. Vo-Dinh, ed. (CRC Press LLC, 2003), chap. I-2, pp. 2–75.
22. G. Nishimura, K. Awasthi, and D. Furukawa, "Fluorescence lifetime measurements in heterogeneous scattering medium," J. Biomed. Opt. **21**, 075013 (2016).
23. E. Alerstam, T. Svensson, , and S. Andersson-Engels, "Parallel computing with graphics processing units for high-speed monte carlo simulation of photon migration," J. Biomed. Opt. **13**, 060504 (2008).
24. G. Nishimura and M. Tamura, "Artefacts in the analyis of temporal response functions measured by photon counting," Phys. Medicine Biol. **50**, 1327–1342 (2005).
25. A. Torricelli, A. Pifferi, L. Spinelli, R. Cubeddu, F. Martelli, S. D. Bianco, and G. Zaccanti, "Time-resolved reflectance at null source-detector separation: Improving contrast and resolution in diffuse optical imaging," Phys. Rev. Lett. **95**, 078101 (2005).
26. F. Martelli, T. Binzoni, A. Pifferi, L. Spinelli, A. Farina, and A. Torricelli, "There's plenty of light at the bottom: statistics of photon penetration depth in random media," Sci. Reports **6**, 27057 (2016).
27. E. M. Sevick, B. Chance, J. S. Leigh, S. Nioka, and M. Maris, "Quantitation of time- and frequency-resolved optical spectra for the determination of tissue oxygenation," Analitical Biochem. **195**, 330–351 (1991).